

ORBITS, MASSES, AND EVOLUTION OF MAIN BELT TRIPLE (87) SYLVIA

JULIA FANG¹, JEAN-LUC MARGOT^{1,2}, AND PATRICIO ROJO³

¹ Department of Physics and Astronomy, University of California, Los Angeles, CA 90095, USA

² Department of Earth and Space Sciences, University of California, Los Angeles, CA 90095, USA

³ Departamento de Astronomía, Universidad de Chile, Santiago, Chile

Received 2012 May 8; accepted 2012 June 25; published 2012 July 16

ABSTRACT

Sylvia is a triple asteroid system located in the main belt. We report new adaptive optics observations of this system that extend the baseline of existing astrometric observations to a decade. We present the first fully dynamical three-body model for this system by fitting to all available astrometric measurements. This model simultaneously fits for individual masses, orbits, and primary oblateness. We find that Sylvia is composed of a dominant central mass surrounded by two satellites orbiting at 706.5 ± 2.5 km and 1357 ± 4.0 km, i.e., about 5 and nearly 10 primary radii. We derive individual masses of $1.484^{+0.016}_{-0.014} \times 10^{19}$ kg for the primary (corresponding to a density of 1.29 ± 0.39 g cm⁻³), $7.33^{+4.7}_{-2.3} \times 10^{14}$ kg for the inner satellite, and $9.32^{+20.7}_{-8.3} \times 10^{14}$ kg for the outer satellite. The oblateness of the primary induces substantial precession and the J_2 value can be constrained to the range of 0.0985–0.1. The orbits of the satellites are relatively circular with eccentricities less than 0.04. The spin axis of the primary body and the orbital poles of both satellites are all aligned within about 2 deg of each other, indicating a nearly coplanar configuration and suggestive of satellite formation in or near the equatorial plane of the primary. We also investigate the past orbital evolution of the system by simulating the effects of a recent passage through 3:1 mean-motion eccentricity-type resonances. In some scenarios this allow us to place constraints on interior structure and past eccentricities.

Key words: minor planets, asteroids: general – minor planets, asteroids: individual (Sylvia)

Online-only material: color figures

1. INTRODUCTION

(87) Sylvia is a triple asteroid residing in the main belt, with a heliocentric semimajor axis of 3.5 AU, an eccentricity of 0.085, and an inclination of 11° relative to the ecliptic. Sylvia’s outer satellite, named Romulus, was discovered in 2001 using the W. M. Keck Telescope (Brown & Margot 2001; Margot & Brown 2001) and was also detected in *Hubble Space Telescope* (*HST*) images (Storrs et al. 2001). The inner satellite, Remus, was not discovered until the advent of improved adaptive optics systems in 2004 using the European Southern Observatory’s Very Large Telescope (VLT) (Marchis et al. 2005). The diameter of the primary has been estimated at ~280 km through shape fits to adaptive optics images (Marchis et al. 2005); this estimate is consistent with stellar occultation observations (Lin et al. 2009). Assuming this primary size, approximate sizes for the individual satellites have been estimated by adopting the same albedo as the primary and measuring each satellite’s brightness relative to the primary. The diameter estimates are ~7 km for Remus and ~18 km for Romulus (Marchis et al. 2005).

Sylvia was the first triple asteroid system announced, even though the triple nature of 2002 CE26 was being actively discussed during the acquisition of the Sylvia observations (Shepard et al. 2006). Additional discoveries of multiples in the solar system have followed. They include near-Earth triples (153591) 2001 SN263 (Nolan et al. 2008) and (136617) 1994 CC (Brozovic et al. 2009), main belt triples Kleopatra (Descamps et al. 2011), Eugenia (Merline et al. 1999; Marchis et al. 2007), Balam (Merline et al. 2002; Marchis et al. 2008), and Minerva (Marchis et al. 2011), and trans-Neptunian systems (47171) 1999 TC36 (Margot et al. 2005; Benecchi et al. 2010), Haumea (Brown et al. 2005, 2006), and the Pluto/Charon system (Weaver et al. 2006).

Following these discoveries, characterization of multiple systems has unearthed a wealth of information about their fundamental physical properties such as masses and densities, dynamical processes, and constraints on formation and evolutionary mechanisms. Such research has been possible because we can derive the masses of the individual components of a triple or higher-multiplicity system by analyzing their mutual gravitational interactions, which is possible in binary systems only when reflex motion is detected (Margot et al. 2002; Ostro et al. 2006; Naidu et al. 2011). These masses in conjunction with size estimates can provide densities. Using this method, Fang et al. (2011) performed a detailed analysis of 2001 SN263 and 1994 CC, including masses, densities, and dynamical evolution. Similarly, work on the Pluto/Charon system and dwarf planet Haumea and its satellites have yielded information about their physical properties, tidal interactions, and evolutionary processes (Lee & Peale 2006; Tholen et al. 2008; Ragozzine & Brown 2009). The high scientific return from studies of binaries and triples has been reviewed by Merline et al. (2002) and Noll et al. (2008).

To date, no such dynamical orbit solution nor detailed analysis has been performed for Sylvia. Previous work by Marchis et al. (2005) approximated the actual orbits of Remus and Romulus with individual two-body fits that included primary oblateness. However, drawbacks of such methods include the failure to account for third-body perturbations as well as the inability to solve for individual component masses. Additional researchers based their studies on the published two-body orbits (Marchis et al. 2005) plus unspecified component mass assumptions to study Sylvia’s long-term evolution (Winter et al. 2009; Frouard & Compere 2012), even though component masses are undetermined and can span several orders of magnitude.

Table 1
Summary of 2011 Observations

UT Date	MJD	Filter	Telescope	Detections
2011 Oct 7	55841.1097	<i>H</i>	VLT	Remus, Romulus
2011 Nov 6	55871.0856	<i>H</i>	VLT	Romulus
2011 Nov 8	55873.1289	<i>H</i>	VLT	Remus, Romulus
2011 Nov 10	55875.0451	<i>H</i>	VLT	Remus, Romulus
2011 Nov 15	55880.0256	<i>H</i>	VLT	Romulus
2011 Nov 16	55881.0466	<i>H</i>	VLT	Remus, Romulus
2011 Nov 20	55885.0460	<i>H</i>	VLT	Romulus
2011 Dec 15	55910.2129	<i>H</i>	Keck	Remus, Romulus
2011 Dec 15	55910.2288	<i>H</i>	Keck	Remus, Romulus
2011 Dec 15	55910.2698	<i>H</i>	Keck	Remus, Romulus
2011 Dec 16	55911.1877	<i>H</i>	Keck	Romulus
2011 Dec 16	55911.2510	<i>H</i>	Keck	Romulus
2011 Dec 17	55912.2615	<i>H</i>	Keck	Remus, Romulus
2011 Dec 18	55913.1972	<i>H</i>	Keck	Romulus
2011 Dec 18	55913.2035	<i>H</i>	Keck	Romulus

Notes. Summary of our 2011 adaptive optics observations at VLT and Keck. Epochs are provided in Universal Time (UT) dates as well as the Modified Julian Date (MJD). Remus is the inner satellite and Romulus is the outer satellite.

In this work, we report additional Keck and VLT imaging data for Sylvia (Section 2). Using primary–satellite separations measured from these data plus published astrometry, we present a fully dynamical three-body orbital and mass solution for Sylvia by accounting for mutually interacting orbits as well as the primary’s nonsphericity (Section 3). Although the orbital periods of the satellites are near a 8:3 ratio, we do not find that the system is currently in such a resonance (Section 4). We also analyze Sylvia’s short-term and long-term future evolution (Section 5). Lastly, we investigate the past orbital evolution of Remus and Romulus by modeling passage through the 3:1 mean-motion resonance (Section 6). A summary of main conclusions is given in Section 7.

2. OBSERVATIONS

We report new observations of Sylvia in 2011 from both Keck and VLT, as well as summarize existing observations taken in 2001–2004 using Keck, *HST*, and VLT. Astrometry derived from these data sets are used for orbit fits described in the next section (Section 3).

2.1. New Data in 2011

Our observations in 2011 are summarized in Table 1. In total, we obtained seven partial nights of service (or “queue”) mode observing at VLT and four partial nights of visitor mode at Keck. At the VLT, we used the NACO (NAOS-CONICA) high-resolution IR imaging camera (Rousset et al. 2003; Lenzen et al. 2003) in its S13 mode using the *H* filter, with a plate scale value reported as $0.013221 \text{ arcsec pixel}^{-1}$.⁴ We used four offset positions in a box pattern, with an integration time of 120 s per offset position. These four offset positions sampled the four quadrants of the CCD to calibrate and mitigate against detector defects. At Keck, we used NIRC2 (Near Infrared Camera 2) imaging in the *H* filter, with a plate scale of $0.009942 \text{ arcsec pixel}^{-1}$.⁵ Our Keck observations used four offset positions in a similar box pattern as with the VLT exposures, with an exposure time of 60 s per offset position. All observations using both VLT and Keck were performed with natural guide star adaptive

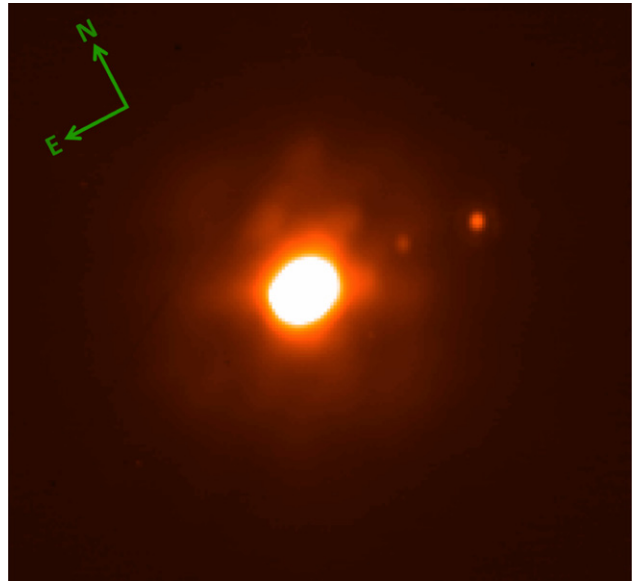


Figure 1. Keck *H*-band adaptive optics image on 2011 December 15 (corresponding modified Julian Date 55910.2129) of Sylvia with its inner satellite Remus and outer satellite Romulus. In this image, the primary–Remus separation is about 0.34 arcsec , and the primary–Romulus separation is about 0.57 arcsec .

(A color version of this figure is available in the online journal.)

optics, using Sylvia as the guide star (its apparent magnitude varied from $V \sim 11.7$ to $V \sim 12.7$ throughout the period of our 2011 observations).

We performed basic data reduction analysis for VLT and Keck images. Each frame (at each dither position) is flat-fielded and its bad pixels are corrected using a bad pixel mask obtained from outlier pixels present in all frames. Sky subtraction is performed by subtracting frames in pairs, where each frame is subtracted by another frame where the target has been offset. We performed subpixel two-dimensional Gaussian fitting to obtain precise centroids of the target in each sky-subtracted frame, and these centroids were used to align and combine all frames into one composite image. See Figure 1 for an example of a composite image obtained using Keck.

At each observation epoch, we detected either one or both satellites (see Table 1). As the satellites orbit the primary, they are occasionally obscured by the bright primary and this occurs most often for the inner satellite Remus. In cases where only one satellite is detected, we determined the identification of the satellite through orbit fitting. An incorrect identification of a satellite is easily shown as an obvious outlier in orbit fits. In all cases examined here, when only one satellite is detected, it is the outer satellite Romulus.

For all satellite detections, we measure the astrometric positions of the satellite relative to the primary by taking the difference between the centroids of the primary and the satellite. Specifically, we measure the position angle (degrees east of north) and separation of the satellite relative to the primary. These measurements are performed on the reduced composite image obtained at each observation epoch. These measurements are provided in Table 2.

2.2. Existing Data from 2001–2004

Publicly available astrometry data sets for Sylvia include Keck data in 2001 (Margot & Brown 2001), *HST* data in 2001 (Storrs et al. 2001), and VLT data in 2004 (Marchis et al.

⁴ <http://www.eso.org/sci/facilities/paranal/instruments/naco/doc>

⁵ <http://www2.keck.hawaii.edu/inst/nirc2/genspecs.html>

Table 2
Astrometry from 2011 Data

Satellite	MJD	P.A. (deg)	Sep. (arcsec)	x (arcsec)	y (arcsec)	σ (arcsec)
Remus	55841.1097	265.07	0.392	0.391	-0.034	0.0132
Remus	55873.1289	75.25	0.226	-0.218	0.057	0.0132
Remus	55875.0451	270.33	0.342	0.342	0.002	0.0132
Remus	55881.0466	87.23	0.381	-0.381	0.018	0.0132
Remus	55910.2129	268.16	0.341	0.341	-0.011	0.0099
Remus	55910.2288	267.49	0.343	0.342	-0.015	0.0099
Remus	55910.2698	267.80	0.325	0.325	-0.012	0.0099
Remus	55912.2615	84.22	0.349	-0.348	0.035	0.0099
Romulus	55841.1097	264.09	0.702	0.698	-0.072	0.0132
Romulus	55871.0856	92.92	0.369	-0.368	-0.019	0.0132
Romulus	55873.1289	271.41	0.606	0.606	0.015	0.0132
Romulus	55875.0451	88.92	0.643	-0.643	0.012	0.0132
Romulus	55880.0256	284.49	0.183	0.177	0.046	0.0132
Romulus	55881.0466	266.17	0.671	0.670	-0.045	0.0132
Romulus	55885.0460	264.34	0.357	0.355	-0.035	0.0132
Romulus	55910.2129	264.30	0.571	0.568	-0.057	0.0099
Romulus	55910.2288	263.66	0.572	0.568	-0.063	0.0099
Romulus	55910.2698	265.11	0.541	0.539	-0.046	0.0099
Romulus	55911.1877	95.41	0.392	-0.391	-0.037	0.0099
Romulus	55911.2510	92.09	0.446	-0.446	-0.016	0.0099
Romulus	55912.2615	78.76	0.423	-0.415	0.082	0.0099
Romulus	55913.1972	272.80	0.528	0.528	0.026	0.0099
Romulus	55913.2035	272.09	0.521	0.521	0.019	0.0099

Notes. Astrometry measured from 2011 data for Remus (inner) and Romulus (outer) at specific MJD epochs. We measured the position angle (P.A.; degrees east of north) and the separation of each satellite relative to the primary. These values are converted to positions x and y , where the positive x -direction is toward the west and the positive y -direction is toward the north. We assign the instrument plate scale as the positional uncertainty σ for x and y .

2005). For the 2004 VLT data, the paper by Marchis et al. (2005) contains their astrometric measurements of the satellites relative to the primary expressed as x - y pairs, where they define x and y as positive in the east and north directions, respectively. However, they failed to indicate the signs (positive or negative) for their x and y measurements of Remus. In addition, at one epoch (MJD 53,253.1738) their published astrometry gives Remus an implausibly large separation from the primary. To fix these inaccuracies, we fit orbits to the astrometric points and have determined the correct signs for their measurements (note that we define x to be positive in the west direction). At epoch MJD 53,253.1738, it appears that they have confused Remus and Romulus, and so we have swapped measurements for these two bodies at that epoch. These corrections, along with astrometry for the Keck and *HST* data in 2001, are given in Table 3.

In total, our baseline of observations spans a decade from 2001 to 2011. For Remus, which is never visible in data obtained prior to 2004, our 2011 observations add an additional 8 epochs to the existing 12 epochs for a total of 20 epochs of astrometry, extending the baseline of observations from about 1 month to 7 years. For Romulus, our 2011 observations add an additional 15 epochs to the existing 30 epochs for a total of 45 epochs of astrometric measurements, extending the baseline of observations from 3 years to 10 years. All of these astrometry positions, given in Tables 2 and 3, are used for dynamical three-body orbit fits described in the next section.

3. ORBITAL AND MASS SOLUTION

We fit a fully dynamical three-body model to the astrometric measurements described in the previous section, taking into account mutually interacting orbits. Our model simultaneously

fits for 16 parameters, including a set of six orbital parameters per satellite (semimajor axis, eccentricity, inclination, argument of pericenter, longitude of the ascending node, and mean anomaly at epoch), three masses for the three bodies, and the parameter J_2 representing the oblateness of the primary. The semimajor axis and eccentricity describe the size and shape of the orbit, both the inclination and longitude of the ascending node describe the orientation of the orbit, the argument of pericenter describes the location of pericenter (minimum radial distance of the orbit), and the mean anomaly at epoch can be used to determine the location of the satellite in its orbit at a particular time.

We describe these fitted parameters in more detail. The orbital elements of each satellite are relative to the primary body and are defined with respect to the Earth equatorial reference frame of epoch J2000. Given that these orbital elements change over time due to perturbations in the three-body system, these are defined as *osculating* orbital elements. They are valid at a specific epoch, MJD 53227.0, corresponding to UT date 2004 August 10 00:00. The fitted masses are derived assuming $G = 6.67 \times 10^{-11} \text{ m}^3 \text{ kg}^{-1} \text{ s}^{-2}$ for the gravitational constant. The primary's non-spherical nature, which can introduce additional non-Keplerian effects, is represented by an oblateness coefficient J_2 . The distribution of mass within the primary can be represented by terms in a spherical harmonic expansion of its gravitational potential, and the quadrupole term J_2 is the lowest-order gravitational moment. J_2 is related to the primary's three principal moments of inertia ($C \geq B \geq A$) as

$$J_2 = \frac{C - \frac{1}{2}(A + B)}{MR^2}, \quad (1)$$

Table 3
Existing Astrometry from 2001–2004 Data

Satellite	MJD	P.A. (deg)	Sep. (arcsec)	x (arcsec)	y (arcsec)	σ (arcsec)	Reference
Remus	53227.3042	-0.411	0.002	0.0132	3
Remus	53249.2470	-0.239	-0.101	0.0132	3
Remus	53249.2532	-0.228	-0.101	0.0132	3
Remus	53251.2985	0.246	0.107	0.0132	3
Remus	53252.3627	0.421	0.000	0.0132	3
Remus	53253.1738	-0.445	-0.025	0.0132	3
Remus	53255.1091	0.435	0.002	0.0132	3
Remus	53256.2886	0.268	-0.072	0.0132	3
Remus	53261.1432	-0.394	0.033	0.0132	3
Remus	53261.2298	-0.430	-0.008	0.0132	3
Remus	53263.2146	0.412	0.004	0.0132	3
Remus	53263.2202	0.416	0.001	0.0132	3
Romulus	51958.4810	97.00	0.564	-0.559	-0.069	0.0168	1
Romulus	51959.3660	60.30	0.425	-0.369	0.211	0.0168	1
Romulus	51959.4200	54.10	0.383	-0.310	0.225	0.0168	1
Romulus	51960.4010	271.90	0.615	0.614	0.020	0.0168	1
Romulus	51962.4070	88.30	0.696	-0.696	0.021	0.0168	1
Romulus	51963.5700	306.00	0.330	0.267	0.194	0.0250	2
Romulus	53227.3042	-0.377	0.144	0.0132	3
Romulus	53246.3105	-0.785	-0.097	0.0132	3
Romulus	53246.3659	-0.755	-0.117	0.0132	3
Romulus	53249.2470	-0.547	0.139	0.0132	3
Romulus	53249.2532	-0.555	0.136	0.0132	3
Romulus	53249.3516	-0.654	0.109	0.0132	3
Romulus	53251.2985	0.763	-0.058	0.0132	3
Romulus	53252.3627	0.156	0.214	0.0132	3
Romulus	53253.1738	-0.791	0.049	0.0132	3
Romulus	53253.3445	-0.834	-0.018	0.0132	3
Romulus	53254.1603	-0.172	-0.214	0.0132	3
Romulus	53255.1091	0.835	0.003	0.0132	3
Romulus	53255.3928	0.793	0.105	0.0132	3
Romulus	53256.2886	-0.272	0.202	0.0132	3
Romulus	53259.2030	0.683	0.165	0.0132	3
Romulus	53261.1432	-0.546	-0.186	0.0132	3
Romulus	53261.2298	-0.449	-0.205	0.0132	3
Romulus	53262.1602	0.724	-0.073	0.0132	3
Romulus	53262.2759	0.786	-0.035	0.0132	3
Romulus	53262.2815	0.791	-0.032	0.0132	3
Romulus	53263.2146	0.221	0.230	0.0132	3
Romulus	53263.2202	0.215	0.231	0.0132	3
Romulus	53297.0193	-0.752	-0.038	0.0132	3
Romulus	53298.0064	0.101	-0.186	0.0132	3

Notes. Existing astrometry measured from 2001–2004 data for Remus (inner) and Romulus (outer) at specific MJD epochs, taken from (1) Margot & Brown 2001; (2) Storrs et al. 2001; and (3) Marchis et al. 2005 (the latter with corrections; see the text). An ellipsis (. . .) means that the value was not reported. Measurements include the position angle (P.A.; degrees Earth of north) and the separation of each satellite relative to the primary. These values can be converted to positions x and y , where the positive x -direction is toward the west and the positive y -direction is toward the north. As in Table 2, we assign the instrument plate scale as the positional uncertainty σ for x and y .

where the denominator is a normalization factor including the primary’s mass M and equatorial radius R (i.e., Murray & Dermott 1999). In all of our fits, the radius R is assumed to be 140 km. The inclusion of J_2 in our fits also requires a primary spin pole direction to be specified, and typically we fix the primary pole to the orbit pole of the most massive satellite.

With a total of 16 parameters and 130 data measurements (Tables 2 and 3), we have 114 degrees of freedom (number of data points minus the number of parameters). We adopt a least-squares approach to this problem by minimizing the chi-square χ^2 statistic, where $\chi^2 = \sum_i (O_i - C_i)^2 / \sigma_i^2$ for a set of

N ($1 \leq i \leq N$) observations with σ_i uncertainties and observed O_i and computed C_i values. We utilize a Levenberg–Marquardt nonlinear least-squares algorithm written in IDL called `mpfit` (Markwardt 2009). With 16 parameters, this is a very computationally intensive problem, given the large amount of parameter space to explore as well as the computationally expensive three-body orbital integrations that need to be performed. Especially for least-squares problems with a large number of parameters, it is impossible to guarantee that a global χ^2 minimum has been found. More often than not, the minimization procedure converged on a local minimum and therefore it was necessary to

re-fit with different starting conditions. In total, we started the fitting procedure with tens of thousands of sets of starting conditions, and we performed up to 20 iterations (equaling hundreds of χ^2 evaluations) for each set of starting conditions.

These starting conditions included plausible ranges of parameter space for fitted parameters. We explored all possible values of eccentricity (0–1), orbital angles (0° – 360°), semimajor axes (500–900 km for Remus and 1100–1500 km for Romulus), and J_2 values (0–0.2). Starting values ranged from on the order of 10^{18} to 10^{20} kg for the primary’s mass and from on the order of 10^{13} to 10^{17} kg for each satellite’s mass. Ranges for satellite masses covered all possible mass values by sampling various size (Remus: ~ 5 –9 km in diameter, Romulus: ~ 14 –22 km in diameter; Marchis et al. 2005) and density (0.1 – 10 g cm $^{-3}$) ranges.

In addition, we also explored various primary spin axis orientations for the primary. This was possible with this data set because the perturbations due to the oblateness of the primary are detectable, and because those perturbations depend on the spin axis orientation. These effects are captured by three fitted parameters: two for the primary spin axis orientation, and one for the value of J_2 . We systematically explored the entire celestial sphere for the primary spin axis orientation, but we also tested specific poles that had been favored by previous studies. These specific spin axis orientations include R.A. = 355° and decl. = 82° (close to satellite orbital poles) suggested from light curve analysis (Kaasalainen et al. 2002), R.A. = 68° and decl. = 78° from a compilation of previous data (Kryszczyńska et al. 2007), and R.A. = 100° and decl. = 62° derived using adaptive optics imaging data (Drummond & Christou 2008). From these fits, we find that primary spin poles misaligned with satellite orbit poles do not provide good solutions (such as poles by Kryszczyńska et al. 2007; Drummond & Christou 2008). Instead, we determined that the best-fit spin axis direction was nearly aligned with the satellites’ orbital poles, which are almost coplanar. As a result, for nearly all fits, we aligned the primary’s spin pole to the orbital pole of the most massive satellite. The fact that both satellites orbit in or near the equator of the primary provides an important constraint on satellite formation mechanisms.

For each set of starting conditions, our orbit-fitting method proceeded as follows. First, we performed N -body numerical integrations using the Mercury integration package (Chambers 1999), which takes into account mutually interacting orbits as well as the effects due to primary oblateness. We used a Bulirsch–Stoer algorithm for our integration method, which is computationally slow but accurate, and we chose an initial time step that samples finer than $1/25$ th of the innermost orbital period. These three-body integrations need to cover all epochs of observation, which span about a decade (2001–2011). From these integrations, we determined the positions and velocities of each satellite relative to the primary at all epochs of observation (corrected for light travel time) by interpolation. The length and resolution of these integrations were the limiting factors in the computational speed of each minimization. Second, we obtained the vector orientation of Sylvia’s position relative to an observer on Earth for all epochs of observation (again, corrected for light time), taking into account aspect variations due to geocentric distance variations and Sylvia’s motion across the sky. Third, we used these orientations to project and compute primary–satellite separations on the plane of the sky at each observation epoch. These computed separations were compared with our observed separations (Tables 2 and 3) to determine the χ^2 goodness-of-

Table 4
Best-fit Parameters and 1σ Uncertainties

Parameter	Best Fit	Formal 1σ	Adopted 1σ
Remus (inner)			
Mass (10^{14} kg)	7.333	± 0.717	+4.7 –2.3
a (km)	706.5	± 0.007	+2.5 –2.5
e	0.02721	± 0.010	+0.013 –0.012
i (deg)	7.824	± 0.667	+0.68 –0.82
ω (deg)	357.0	± 15.14	...
Ω (deg)	94.80	± 5.000	+5.2 –5.8
M (deg)	261.0	± 13.43	...
P (days)	1.373	...	+0.010 –0.010
Romulus (outer)			
Mass (10^{14} kg)	9.319	± 5.406	+20.7 –8.3
a (km)	1357	± 0.059	+4.0 –4.0
e	0.005566	± 0.004	+0.005 –0.004
i (deg)	8.293	± 0.210	+0.21 –0.29
ω (deg)	61.06	± 18.74	...
Ω (deg)	92.60	± 1.339	+2.9 –1.6
M (deg)	197.0	± 18.75	...
P (days)	3.654	...	+0.025 –0.024
Primary			
Mass (10^{19} kg)	1.484	± 0.00017	+0.016 –0.014
J_2	0.09959	± 0.00084	+0.0004 –0.0010
R.A. (deg)	2.597	± 1.339	+3.4 –1.6
Dec. (deg)	81.71	± 0.210	+0.29 –0.71

Notes. Best-fit parameters including individual masses, orbital parameters (semimajor axis a , eccentricity e , inclination i , argument of pericenter ω , longitude of the ascending node Ω , and mean anomaly at epoch M), primary oblateness J_2 , and primary spin pole (R.A. and decl.). These orbital elements are valid at epoch MJD 53227 in the equatorial frame of J2000. We derived an effective orbital period P from the best-fit values of semimajor axis and mass of the considered satellite plus all interior masses. Two types of uncertainties are listed: formal 1σ statistical errors are derived from the least-squares covariance matrix, and adopted 1σ errors are obtained for select parameters through a more rigorous method (see the text). For parameters ω and M with no adopted 1σ errors, we recommend using the formal 1σ errors.

fit statistic. These methods benefit from the heritage of over a decade of work on orbit fitting as well as our work on fitting three-body models to data sets of triples, including near-Earth asteroids (Fang et al. 2011).

Table 4 shows the best-fit orbit solution. The chi-square is 73.55, and with 114 degrees of freedom, this corresponds to a reduced chi-square of 0.6452. This indicates that the fit is very good, and that uncertainties were likely slightly overestimated. This best-fit solution is also visually illustrated in an orbit diagram in Figure 2, where the orbits are projected onto the primary’s equatorial plane. Residuals of the best-fit solution are shown in Figure 3 for Remus and Figure 4 for Romulus, where each figure’s panel shows the residuals for a particular year of observation (2001, 2004, or 2011). The residual is defined as $\chi_i = (O_i - C_i)/\sigma_i$ for observation epoch i .

There are two types of 1σ uncertainties given in Table 4: formal and adopted. The *formal* 1σ uncertainties are obtained using the covariance matrix resulting from the least-squares fitting procedure. These formal 1σ uncertainties may not always be accurate representations of the actual uncertainties. Accordingly, the *adopted* 1σ uncertainties are obtained through a more

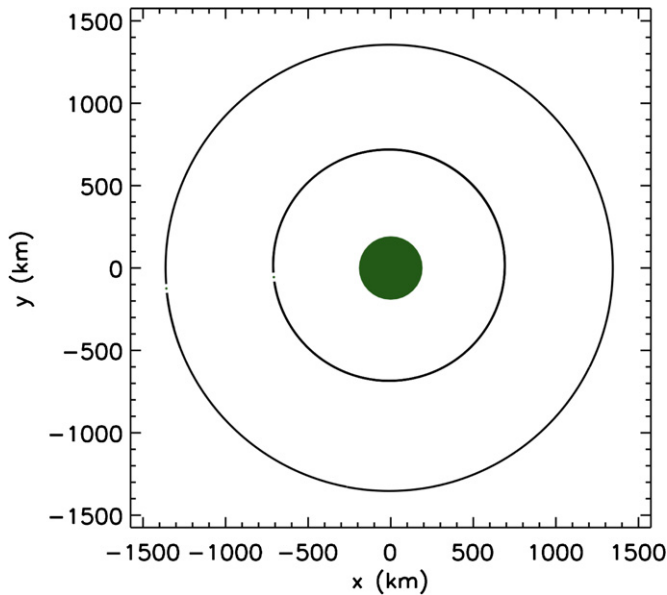


Figure 2. Diagram of best-fit orbits for satellites Remus (inner) and Romulus (outer), projected onto the primary's equatorial plane. These orbits show the actual trajectories from numerical integrations. The relative sizes of the bodies are shown to scale using green circles, assuming these diameters: 10.6 km for Remus, 10.8 km for Romulus, and 280 km for the primary. All bodies are located at their positions at MJD 53227 with the primary centered on the origin. (A color version of this figure is available in the online journal.)

rigorous method by determining each parameter's 1σ confidence levels (e.g., Cash 1976; Press et al. 1992). To determine each parameter's uncertainties, we hold the parameter fixed at a range of plausible values while simultaneously fitting for all other parameters. Since one parameter is held fixed at a time, a 1σ confidence region is prescribed by the range of solutions that yield chi-square values within 1.0 of the lowest chi-square. This is a computationally intensive process, and we performed this method to determine uncertainties for the primary's pole (R.A. and decl.) as well as for each fitted parameter with the exception of the arguments of pericenter and mean anomalies at epoch. We consider the adopted uncertainties to be more accurate representations of the actual uncertainties than the formal uncertainties. We note that these adopted uncertainties do not preclude any systematic errors that may have occurred, such as during the measurement of astrometry from the images.

Most solve-for parameters are well constrained by the data, with formal uncertainties of 10% or less, and as low as $\sim 1\%$ for the mass and oblateness of the primary. One notable exception is the mass of Romulus. The formal uncertainty on this parameter amounts to $\sim 60\%$ of the nominal value, indicating that it is not well constrained by the data. As for orbit pole orientations, they are determined to ~ 1.5 deg uncertainty (1σ) for Remus and ~ 1 deg for Romulus, and the primary spin axis orientation is determined to ~ 1 deg. Given the near-circular nature of the orbits, the arguments of pericenter ω and hence mean anomalies at epoch M are not well defined (but the satellite positions, or $\omega + M$, are in fact well defined).

The best-fit orbital solution indicates that the satellites follow relatively circular orbits at semimajor axes of about 5 and nearly 10 primary radii. The mutual inclination (relative inclination) between the orbital planes of the satellites is $0^{\circ}.56_{-0.5}^{+1.5}$. The low mutual inclination indicates that the orbital planes are nearly coplanar. This alignment supports a satellite formation mechanism in which the satellites would tend to remain close

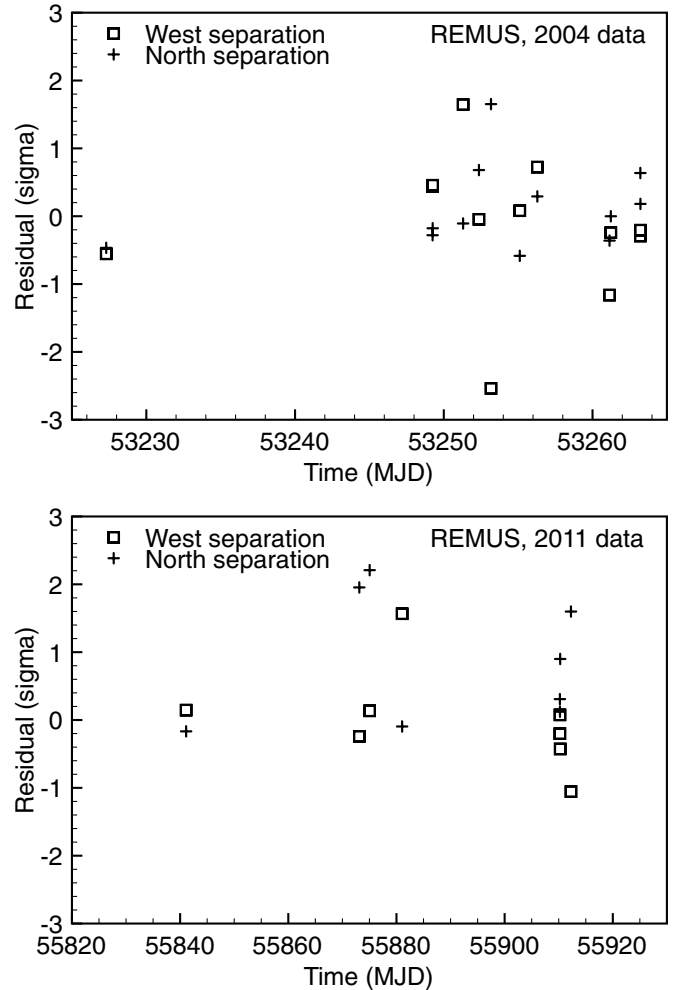


Figure 3. Residuals (O-C) for Remus-Sylvia angular separations in the west and north directions corresponding to the best-fit orbit (Table 4). The two panels represent distinct epochs of observations (2004 and 2011).

to the equatorial plane of the primary (e.g., a subcatastrophic collision). The alignment is likely indicative of formation conditions rather than evolution, as tidal damping of inclinations can be a lengthy process. Assuming various models (monolithic or rubble pile) for tidal dissipation, inner satellite Remus could take on the order of 10^8 years up to the age of the solar system to damp from 2 deg to 1 deg.

Information about size, shape, and density can be derived from our best-fit orbital solution. We obtain a density of $1.29 \pm 0.39 \text{ g cm}^{-3}$ for the primary by assuming a diameter of 280 km (lacking realistic error bars on the size of the primary, we assumed volume uncertainties of 30%). The density error is dominated by the volume error since the mass of the primary is known to $\sim 1\%$. The primary is also oblate, with a well-constrained J_2 value of about 0.09959 which corresponds to an axial ratio $c/a = 0.7086$ if we assume equatorial symmetry and uniform density. Size estimates for Remus and Romulus can be obtained by assuming that they have a bulk density equal to that of the primary, and by considering the adopted 1σ confidence interval of satellite masses. We find radii of $\sim 4.5\text{--}6.1$ km for Remus and $\sim 2.6\text{--}8.2$ km for Romulus. These ranges would have to be modified if the density of the primary or of the satellites was different from the nominal value assumed here, but only slightly as the dependence is $\rho^{-1/3}$.

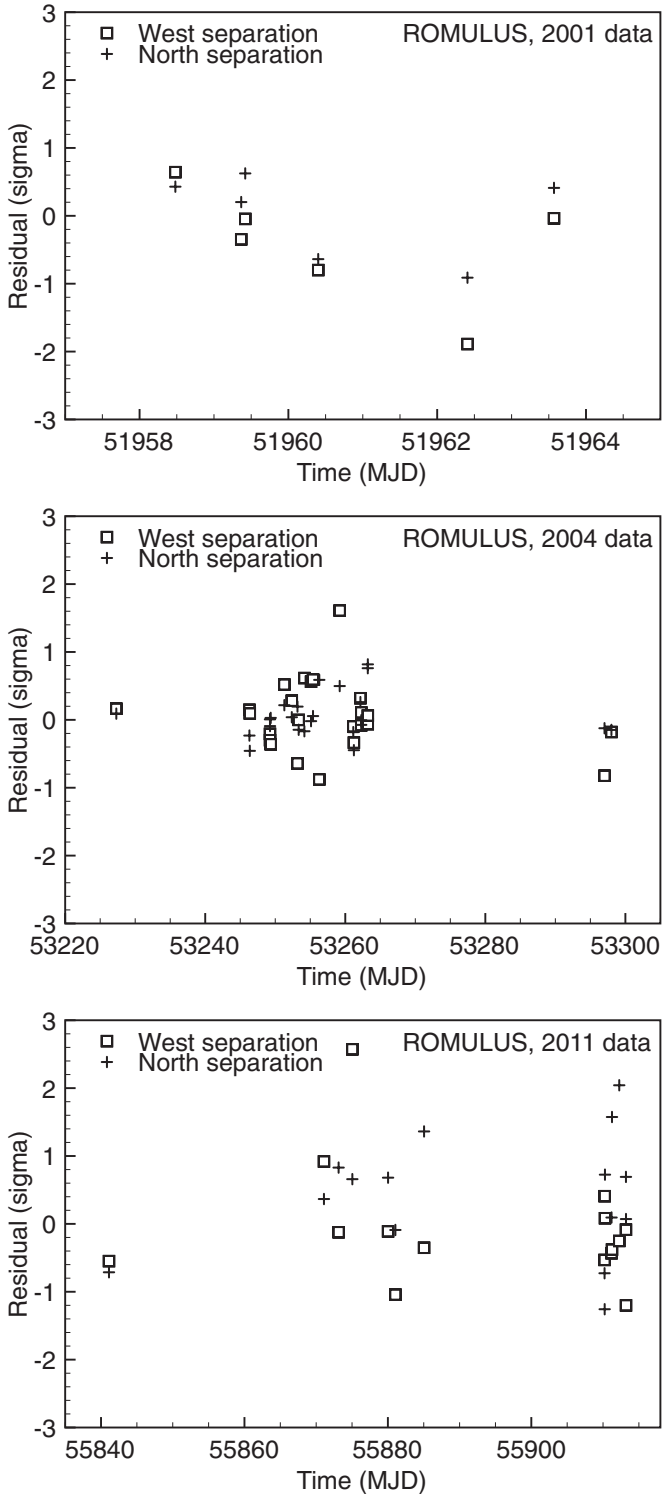


Figure 4. Residuals (O-C) for Romulus-Sylvia angular separations in the west and north directions corresponding to the best-fit orbit (Table 4). The three panels represent distinct epochs of observations (2001, 2004, and 2011).

We compare our best-fit solution in Table 4 to the solution previously reported by Marchis et al. (2005). We find close agreement in semimajor axes (within uncertainties). The eccentricities are marginally consistent. Orbital plane orientations differ by about $\lesssim 2$ deg. The largest discrepancy between our orbital solutions is the value of J_2 . Our fits yield a very well-constrained J_2 value with a 1σ confidence range of 0.0985–0.1.

Marchis et al. (2005) report two estimates for J_2 of 0.17 ± 0.05 and 0.18 ± 0.01 , inconsistent with our value. Using axial ratios from light curve analysis (Kaasalainen et al. 2002) and a uniform density assumption, we find $J_2 = 0.1$, in excellent agreement with our dynamical value.

There are several possibilities to explain the discrepancies between our orbital solutions and those of Marchis et al. (2005). First, our orbital fits are based on a much longer baseline of observations (2001–2011) than their data set (only 2004). Second, our orbital solution is the result of fully dynamical, N -body orbital fits that simultaneously fitted for all parameters in the system, using numerical integrations taking into account mutually interacting orbits and primary oblateness. The fit obtained by Marchis et al. (2005) used two-body approximations (one satellite’s orbit is fit at a time, ignoring effects by the other satellite). These differences in data set and technique allowed us to obtain better-constrained orbital parameters with smaller uncertainties as well as individual masses, which were not previously known.

4. EXAMINATION OF MEAN-MOTION RESONANCE OCCUPANCY

The orbital periods (ratio ≈ 2.661) of our best-fit solution in Table 4 have a ratio near 8:3 (ratio ≈ 2.667). To determine resonance occupation, we search for librating resonance arguments using a general form of the resonance argument (Murray & Dermott 1999)

$$\phi = j_1\lambda_2 + j_2\lambda_1 + j_3\varpi_2 + j_4\varpi_1 + j_5\Omega_2 + j_6\Omega_1. \quad (2)$$

In Equation (2), ϕ is the resonant argument or angle, λ is the mean longitude, ϖ is the longitude of pericenter, and Ω is the longitude of the ascending node. Subscripts 1 and 2 represent the inner and outer satellites, respectively. The j_i values (where $i = 1-6$) are integers and their sum must equal zero (d’Alembert’s rule). For the fifth-order 8:3 mean-motion resonance, $j_1 = -8$ and $j_2 = 3$ so we search through integer values (-30 to $+30$) of the remaining j_i values to determine if there is libration of the resonant argument over timescales ranging from 10 to 100 years. To perform this search, we determined the evolution of the relevant angles in Equation (2) using three-body numerical integrations with the best-fit orbital, mass, and J_2 solution in Table 4. We do not find any librating resonance arguments, and therefore we conclude that the current system is not in the 8:3 mean-motion resonance.

5. SHORT-TERM AND LONG-TERM STABILITY

In this section, we discuss the results of forward N -body integrations of the best-fit orbital solution at MJD 53,227 given in Table 4. We perform short-term (50 yr) and long-term (1 Myr) simulations to determine how the orbital elements fluctuate with time and to assess the stability of this three-body system. Both short-term and long-term integrations are performed using a Bulirsch–Stoer algorithm in Mercury (Chambers 1999) with an initial time step of 0.05 days, and include the gravitational effects of the three bodies and the primary’s oblateness. For long-term integrations, we also include the effect of solar gravitational perturbations.

The results of our short-term integrations are shown in Figure 5. This figure illustrates how the semimajor axes and eccentricities of both satellites evolve over a span of 50 years. From this figure, we can compute the mean value of orbital elements, in contrast to the osculating orbital elements provided

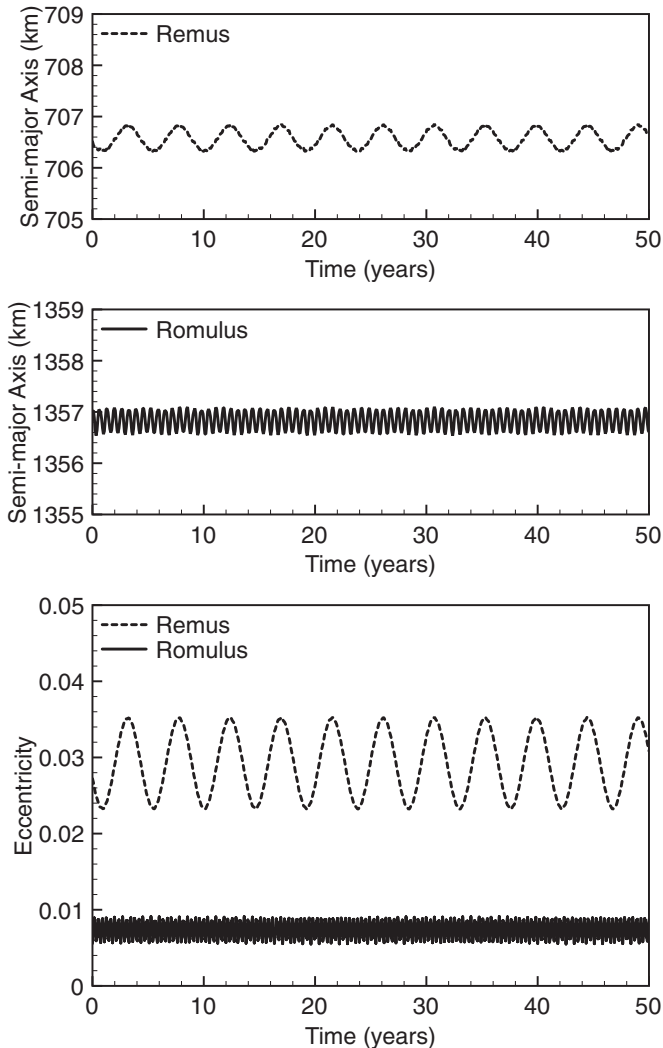


Figure 5. Variation of semimajor axis and eccentricity over a 50 year time span.

in Table 4 that are valid at the specific epoch of MJD 53,227.0. The semimajor axes for both Remus and Romulus have small oscillations spanning less than 1 km and have mean values of 706.57 km and 1356.83 km, respectively. The mean eccentricity values are 0.029 for Remus and 0.0074 for Romulus. The eccentricity variations are especially apparent for Remus, whose eccentricity can vary from 0.023 to 0.035. These short-period fluctuations are due to the effect of the oblateness J_2 of the primary. The force due to the primary’s gravitational field can be modified to account for primary J_2 , and this modified force affects a satellite’s orbit by inducing short-period fluctuations in the semimajor axis, mean motion, eccentricity, and mean anomaly. Its effect on eccentricity can be mathematically approximated as (Brouwer 1959; Greenberg 1981)

$$\Delta e \approx 3J_2(R_p/a)^2, \quad (3)$$

where Δe is the maximum eccentricity excursion from minima to maxima and R_p is the primary’s radius. Plugging in values of $J_2 = 0.09959$, $R_p = 140$ km, and $a = 706.57$ km (Remus) and 1356.83 km (Romulus), we compute $\Delta e \approx 0.0117$ for Remus and $\Delta e \approx 0.00318$ for Romulus. These values are consistent with the maximum excursions seen in numerical simulations that are plotted in Figure 5. Since Remus has a smaller separation ($\sim 5 R_p$) from the primary than Romulus

($\sim 9.7 R_p$), its perturbation by primary J_2 is stronger, hence the larger eccentricity variations seen in Figure 5. As for precession of the orbital planes, there is significant precession due to J_2 and the presence of the other satellite. For example, Remus’ longitude of pericenter precesses $\sim 560^\circ$ per year due to J_2 and $\sim 1^\circ$ per year due to Romulus.

The results from our long-term integrations show that this triple system is stable over 1 Myr, and the variations in semimajor axis and eccentricity do not noticeably exceed the fluctuations shown in Figure 5 for the short-term integrations. Accordingly, we find that Sylvia is in a very stable configuration, as suggested by its near circular and coplanar orbital state. We find that the inclusion of the Sun’s gravitational effect does not appreciably affect the semimajor axes and eccentricities of Sylvia’s satellite orbits. If we consider Sylvia’s Hill sphere of gravitational influence, defined as $r_{\text{Hill}} = a_\odot(M/(3M_\odot))^{1/3}$ (a_\odot is the heliocentric semimajor axis, M is the primary’s mass, and M_\odot is the mass of the Sun), we calculate that the satellites orbit at $\sim 1\%$ and $\sim 2\%$ of the Hill radius. As a result, they are both well within the primary’s sphere of gravitational dominance over the Sun.

Our stability results are in agreement with two previous investigations on Sylvia’s stability. Winter et al. (2009) performed stability analyses of the system, including the effects of the Sun and Jupiter. They find that Sylvia is not stable unless the primary has at least a minimal amount of oblateness (0.1% of their assumed primary J_2 of 0.17). They show that the inclusion of primary oblateness gives rise to a secular eigenfrequency that is much faster than those induced by other gravitational perturbations, which provides a stabilizing effect on the satellites’ orbital evolution. Frouard & Compere (2012) investigated Sylvia’s short-term (20 years) and long-term evolution (6600 years) including the primary’s non-sphericity (assuming $J_2 \approx 0.14$) and solar perturbations. They also varied the semimajor axis and eccentricity of the satellites’ orbits to determine the extent of their stability zones. They find that the current configuration of the system lies in a very stable zone. Authors from both papers (Winter et al. 2009; Frouard & Compere 2012) mention that the effect of Jupiter is negligible compared to the effect of the Sun.

6. EVOLUTION OF ORBITAL CONFIGURATION

In this section, we investigate the past orbital evolution of Remus and Romulus. We find that tidal perturbations can cause the orbits to evolve and to cross mean-motion resonances. This resonance passage may perturb orbits by increasing eccentricities. First we discuss how tidal processes likely caused the satellites to encounter the 3:1 mean-motion resonance in their past, then we describe our numerical modeling methods, and lastly we present plausible past evolutionary pathways as suggested by our simulation results.

6.1. Tidal Theory

Tidal evolution can cause the semimajor axis of an orbit to expand due to tides raised on the primary by its satellite (Goldreich 1963; Goldreich & Soter 1966). Tides raised on the satellite by the primary have an insignificant effect on the semimajor axis. The rate of semimajor axis evolution is given as

$$\frac{da}{dt} = 3 \frac{k_p}{Q_p} \frac{M_s}{M_p} \left(\frac{R_p}{a} \right)^5 na, \quad (4)$$

where a is the semimajor axis, k is the tidal Love number, Q is the tidal dissipation factor, M is the mass, R is the radius, and n is the mean motion. The subscripts p and s denote quantities for the primary and satellite, respectively. It is likely that tidal evolution is causing the orbits of Remus and Romulus to expand, and that their orbits were in a more compact configuration in the past. We discuss the relative importance of tides compared to another important evolutionary process (BYORP) at the end of this subsection.

We expect that orbital expansion by tides is causing the relative orbits of Remus and Romulus to slowly converge toward each other. Two orbits are converging if \dot{a}_1/\dot{a}_2 is greater than one, and here subscripts 1 and 2 represent Remus (inner) and Romulus (outer), respectively. Using Equation (4), we can express this criterion as

$$\frac{\dot{a}_1}{\dot{a}_2} = \frac{M_1}{M_2} \left(\frac{a_2}{a_1} \right)^{11/2} > 1. \quad (5)$$

Assuming best-fit values for the semimajor axes of Remus and Romulus (Table 4), their orbits are currently converging as long as their mass ratio satisfies $M_1/M_2 > 0.0276$. Taking into account the range of the 1σ adopted confidence interval in masses (from Table 4), we find that this ratio is satisfied in all cases and therefore we expect that their orbits are converging. The steep dependence of tidal evolution on semimajor axis causes the orbit of Remus to expand much faster than the orbit of Romulus. Given that their orbits are slowly converging over time, we can determine the most recent mean-motion resonance passage encountered by the satellites. By considering all first-, second-, third-, and fourth-order resonances (where a $p+q:p$ resonance is q th order), we expect that the most recent resonance encountered by the system is the second-order 3:1 resonance. Accordingly, in our analysis here we focus on the 3:1 resonance and its effect on the satellites' eccentricity evolution.

We describe how tidal evolution causes the eccentricity of an orbit to increase or decrease. This is a competing process between the opposing effects of tides raised on the primary (eccentricity increases) and tides raised on the satellite (eccentricity decreases). These two opposing effects are contained in two terms in the equation (Goldreich 1963; Goldreich & Soter 1966)

$$\frac{de}{dt} = \frac{57}{8} \frac{k_p}{Q_p} \frac{M_s}{M_p} \left(\frac{R_p}{a} \right)^5 ne - \frac{21}{2} \frac{k_s}{Q_s} \frac{M_p}{M_s} \left(\frac{R_s}{a} \right)^5 ne, \quad (6)$$

which gives the evolution of eccentricity e . The variables and subscripts in Equation (6) are the same as for Equation (4).

We discuss models for the tidal Love number k in Equations (4) and (6) used for calculations of tidal evolution in asteroids. These models are dependent on the asteroid's radius R . First, we consider the monolith model, where

$$k \approx \frac{1.5}{1 + 2 \times 10^8 \left(\frac{1 \text{ km}}{R} \right)^2}, \quad (7)$$

and this model is appropriate for asteroids that are idealized as uniform bodies with no voids (Goldreich & Sari 2009). Second, we consider a rubble pile model by Goldreich & Sari (2009) with the following Love number formalism:

$$k \approx 1 \times 10^{-5} \left(\frac{R}{1 \text{ km}} \right). \quad (8)$$

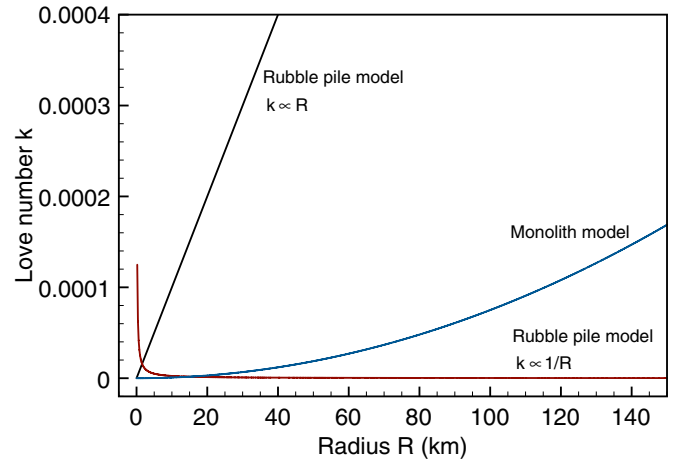


Figure 6. Tidal Love number models (Equations (7)–(9)) as a function of radius. Intersections between the $k \propto 1/R$ model and the other two models occur at 1.58 km and 14.94 km.

(A color version of this figure is available in the online journal.)

Rubble pile models are appropriate for asteroids idealized as gravitational aggregates. Another rubble pile model is given by Jacobson & Scheeres (2011), where

$$k \approx 2.5 \times 10^{-5} \left(\frac{1 \text{ km}}{R} \right). \quad (9)$$

Equation (9) was obtained by fitting to the configurations of known asteroid binaries and assuming they are in an equilibrium state with tidal and BYORP effects canceling each other. Comparisons between these three Love number models are given in Figure 6.

Here we assume that tidal evolution is a dominant process and we do not analyze other evolutionary processes such as BYORP perturbations. BYORP is a radiative effect that is predicted to cause orbital evolution of a synchronous satellite on short timescales (Ćuk & Burns 2005; Ćuk 2007) and has not been observationally verified yet. BYORP effects dominate at larger semimajor axes, and tides dominate at smaller semimajor axes (Jacobson & Scheeres 2011). Tides result in an increase of the semimajor axes, but BYORP can result in an increase or a decrease, depending on the shapes of the satellites, which are unknown. For the purpose of our evolution calculations, the relevant semimajor axis rate is the *relative* migration rate of the satellites, and we compare the contributions by tides and BYORP by calculating $|(\dot{a}_{\text{tides},1} - \dot{a}_{\text{tides},2})/(\dot{a}_{\text{byorp},1} - \dot{a}_{\text{byorp},2})|$, with subscripts 1 = inner and 2 = outer. We find that this quantity is ~ 1.4 – 3.3 (taking into account whether BYORP acts in the same or opposite directions for both satellites), and therefore we expect that tidal evolution will dominate the relative rate of the satellites' orbits as they converge. This calculation assumes current semimajor axes, $Q_p = 100$, and a monolith tidal Love number model for the primary. If BYORP causes the orbits of the satellites to converge, then joint evolution by tides and BYORP will result in a higher relative migration rate than the tides-only evolution considered here. If BYORP works against tides, then their joint evolution will be slower. Given the order-of-magnitude uncertainties already inherent in unknown tidal parameters such as Q and k as well as uncertainties in whether BYORP will expand or contract the satellites' orbits, we do not include the effects of BYORP in our simulations.

6.2. 3:1 Eccentricity-type Resonances

The 3:1 mean-motion resonance is the most recent low-order resonance encountered by Remus and Romulus, and here we briefly describe the relevant eccentricity-type resonances that can affect orbital eccentricities. We do not consider 3:1 inclination-type resonances in our simulations. There are three eccentricity-type resonances for the 3:1 mean-motion resonance: e_2^2 resonance which perturbs only the outer satellite's eccentricity, e_1e_2 mixed resonance which perturbs both satellites' eccentricities, and the e_1^2 resonance which perturbs only the inner satellite's eccentricity. Subscripts 1 and 2 represent Remus (inner) and Romulus (outer), respectively.

The relevant resonance arguments ϕ for these three 3:1 eccentricity resonances are (e.g., Murray & Dermott 1999)

$$e_2^2: \quad \phi = 3\lambda_2 - \lambda_1 - 2\varpi_2, \quad (10)$$

$$e_1e_2: \quad \phi = 3\lambda_2 - \lambda_1 - \varpi_1 - \varpi_2, \quad (11)$$

$$e_1^2: \quad \phi = 3\lambda_2 - \lambda_1 - 2\varpi_1, \quad (12)$$

where λ is the mean longitude and ϖ is the longitude of pericenter. Occupation of any of these resonances requires libration of the considered resonance argument (exact resonance occurs when $\dot{\phi} = 0$). Note that $\lambda = n$, where n is the mean motion and is related to the semimajor axis.

The resonance arguments given in Equations (10)–(12) are listed in the order that these resonances are encountered due to tidal migration: first the e_2^2 (at $a_1/a_2 \approx 0.481$), then the e_1e_2 (at $a_1/a_2 \approx 0.483$), and lastly the e_1^2 (at $a_1/a_2 \approx 0.485$), where the resonance locations a_1/a_2 must be adjusted depending on the exact starting values of a_1 and a_2 . These resonances are not located at the same semimajor axes; differentiation of Equations (10)–(12) shows that the various resonant arguments will librate at different values of n_1 and n_2 . Such “resonance splitting” occurs because perturbations such as the effect of primary J_2 , and to a lesser degree (in this case, 2–3 orders of magnitude smaller), secular perturbations, causes ϖ of the satellites to precess at different rates. In Section 6.4, we will discuss the capture of Remus and Romulus into any of these resonances. Next, we describe our methods regarding the implementation of tidal effects using direct N -body integrations.

6.3. Methods

Our methods and implementation for simulating a 3:1 resonant passage due to tidal migration are as follows. We use an N -body integrator with a variable time step Bulirsch–Stoer algorithm from Mercury (Chambers 1999). We implement additional terms in the equations of motion due to the effects of tides on semimajor axis and eccentricity by following the numerical methods described in Appendix A of Lee & Peale (2002). Specifically, we used Equations (4) and (6) to model the tidal evolution in a time of a and e . We have tested our implementation by reproducing results in Lee & Peale (2002) as well as matching the analytical expectations (Equations (4) and (6)) of semimajor axis drift and eccentricity evolution outside of resonance.

Actual tidal timescales can be computationally prohibitive, and we incorporate a “speed up” factor to artificially increase the rate of tidal evolution in our simulations. Such speed up factors have also been numerically implemented in previous studies of tidal migration (i.e., Ferraz-Mello et al. 2003; Meyer & Wisdom

2008; Zhang & Nimmo 2009), where they adopted values up to 1000 and found that their results were not sensitive to the choice of speed up factor in the range 1–1000. In our implementation, we incorporate a speed up factor by multiplying Equations (4) and (6) by typical speed up factors of 100–1000. In agreement with previous studies, we find that our results are not sensitive to the choice of speed up factors up to 1000 for select test cases.

We integrate the system for artificial durations of 1–10 Myr, which, because of the speed up factors, represent 1 Gyr of tidal evolution. Our figures show the tidal evolution timescale, not the artificial timescale used in the integrator. The 1 Gyr timescale is constrained by the lifetime of Sylvia’s satellite system. Work by Vokrouhlický et al. (2010) investigating the collisionally born asteroid family related to Sylvia suggests that the family members (and hence the satellites) are at least 10^8 years old. We can also estimate the lifetime of the satellites by considering how much time would pass before a collision occurred between one of the satellites and another main belt asteroid. We estimate this timescale to be roughly 10^9 years (Farinella et al. 1998; Bottke et al. 2005) by assuming that the smallest satellite has a diameter of 10.6 km, as suggested by our orbital fit analysis (Section 3). Accordingly, we consider 1 Gyr to be a reasonable time within which tidal evolution can have taken place, and we typically do not run simulations longer than 1 Gyr.

For the default set of initial conditions in our simulations, the masses of all bodies and primary oblateness (J_2) are taken from Table 4. Simulations are started with coplanar and nearly circular ($e = 0.001$) orbits. Angles for the argument of pericenter and mean anomaly are given a random value from 0° to 360° . Initial semimajor axes for Remus and Romulus are 654 km and 1352.5 km, just inside the 3:1 resonance location. To simulate tidal evolution, we also need to adopt values for the Love number k and tidal dissipation factor Q . To calculate the Love number, we use the tidal monolith model for these bodies (see, e.g., Goldreich & Sari 2009). For all bodies, we assume $Q = 100$, a reasonable assumption for rocky monoliths.

We also ran an additional set of simulations where we varied the initial eccentricities of both satellites (0.001–0.050), primary J_2 (5%–10% lower and higher than its best-fit value), satellite masses that spanned the range of adopted 1σ confidence intervals (low–high, low–low, high–low, and high–high combinations), and repeats of the nominal configuration for additional randomized initial angles of the argument of pericenter and mean anomaly. We did not specifically vary the tidal quantity k/Q , as the effect of varying k/Q is the same as varying the speed up factor since they both contribute linearly to \dot{a} and \dot{e} . We describe our results in the next subsection.

6.4. Results: Evolutionary Pathways

Here, we describe the results stemming from our simulations of a 3:1 resonant passage between Remus and Romulus. These results suggest three evolutionary pathways: capture into resonance with no escape, temporary capture followed by escape, and no capture. We describe each of these evolutionary pathways in the following paragraphs.

6.4.1. Capture with no Escape

This scenario, where resonant capture occurs with no escape during the 1 Gyr evolution, was typically observed for the e_2^2 resonance. An example of such evolution is shown in Figure 7. Given that (1) the satellites are not currently observed in 3:1 resonance and (2) these simulations show no escape from such resonant capture within a reasonable system lifetime of 1 Gyr,

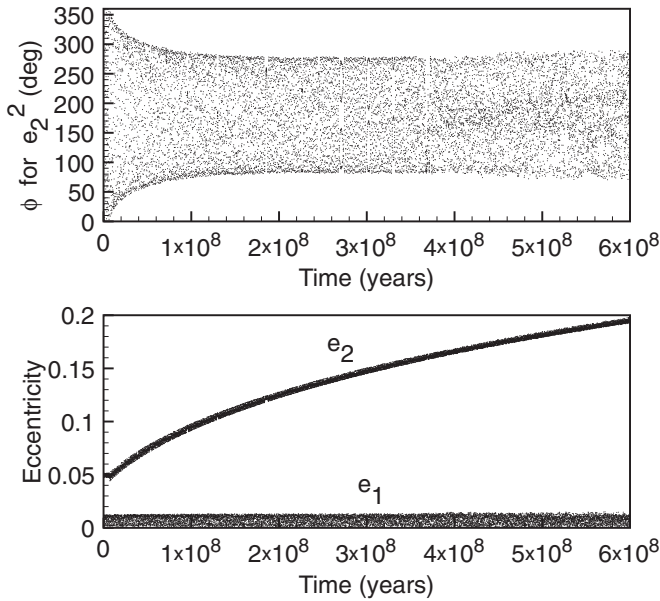


Figure 7. Example of a simulation with resonant capture into e_2^2 and no escape. Dots show results from numerical simulations for the libration angle ϕ and eccentricity e as a function of time. Subscripts 1 and 2 represent the inner and outer satellites, respectively. The simulation was started at $a_1/a_2 = 654.0/1352.5 = 0.4835$ and reached the e_2^2 resonance at $a_1/a_2 = 655.2/1352.5 = 0.4844$, roughly 8 Myr after the start of the simulation. The outer satellite's eccentricity will continue to increase due to resonance effects, but the tidal damping effects will increase as the eccentricity grows, such that an equilibrium value for e may be reached.

we conclude that this evolutionary pathway did not occur and we do not discuss it further.

6.4.2. Temporary Capture Followed by Escape

In this event, resonant capture occurs and is followed by eventual escape due to growth of the resonant argument. This was a common outcome for each of the three types of resonances. Examples of such evolution are shown in Figure 8. Final eccentricities at the end of our simulations ranged from their initial values up to ~ 0.3 . We are unable to place lower bounds on the final eccentricities because we cannot assess how long the satellites may have been captured in the resonance. If high eccentricities resulted from temporary resonance capture, then sufficient eccentricity damping may have subsequently occurred to bring high post-resonance eccentricities to low observed eccentricities.

We investigated whether such eccentricity damping was possible within a conservative time frame of 1 Gyr. To do so, we integrated the \dot{a} and \dot{e} tidal expressions in Equations (4) and (6) and considered all Love number models (Equations (7)–(9)), various post-resonance eccentricities up to 0.25, and tidal dissipation Q values (10–1000). We assumed that both satellites had densities equal to that of the primary (1.29 g cm^{-3}).

For Remus, we find that eccentricity damping to observed values is only possible if we assume rubble pile Love number models (either $k \propto R$ or $k \propto 1/R$) for Remus (there is no restriction on the primary). If we make this assumption, damping to observed values is possible by adopting reasonable values of $Q_p = 100$ and $Q_s = 10$ –100. When we assume that Remus is monolithic, even when we adopt very favorable conditions for eccentricity damping,⁶ tidal damping to its observed value

⁶ $Q_p = 1000$ and $Q_s = 10$. Inspection of Equation (6) shows that damping can be sped up by making Q_p/Q_s as large as possible.

is only possible if we assume a post-resonance eccentricity of ~ 0.032 or less. These calculations suggest that if its post-resonance eccentricity exceeded ~ 0.032 , it is likely that Remus may have an interior structure more akin to a rubble pile aggregate than a monolithic body.

For Romulus, damping to observed eccentricities is possible only if the eccentricity was barely affected while in the resonance (as well as assuming favorable dissipation conditions: $Q_p = 1000$ and $Q_s = 10$). If the eccentricity reached even modest values (~ 0.023) we find that none of the Love number models and reasonable $Q = 10$ –1000 values can damp eccentricities to even the highest possible observed eccentricity (0.011) allowed by our fit uncertainties. Therefore, if temporary capture in the 3:1 occurred, it must not have lasted long enough for the eccentricity of Romulus to reach values of ~ 0.023 . While such a scenario does not entirely rule out the e_2^2 and e_1e_2 resonances, it does seem to place bounds on the acceptable increase in eccentricity due to the 3:1 resonance.

6.4.3. No Capture

In this case, all eccentricity-type resonances are encountered and none result in capture. For orbits that are slowly converging toward each other, capture is possible depending on their initial eccentricities. When the pre-encounter eccentricity is below a critical eccentricity, capture is guaranteed. When the pre-encounter eccentricity exceeds a critical eccentricity, capture becomes a probabilistic event. For the 3:1 resonance, critical eccentricities can be estimated as (Murray & Dermott 1999)

$$e_{1,\text{crit}} = \left[\frac{3}{32f_1} \left(3^{2/3} \frac{M_p}{M_2} + 3^{4/3} \frac{M_1}{M_2} \frac{M_p}{M_2} \right) \right]^{-1/2}, \quad (13)$$

$$e_{2,\text{crit}} = \left[\frac{3}{32f_2} \left(3^{2/3} \frac{M_2}{M_1} \frac{M_p}{M_1} + 9 \frac{M_p}{M_1} \right) \right]^{-1/2}, \quad (14)$$

where subscripts p , 1, and 2 represent the primary, Remus, and Romulus, respectively. The f_1 and f_2 terms represent functions of Laplace coefficients $b_{1/2}^{(j)}(\alpha)$. They are (e.g., see Murray & Dermott 1999)

$$f_1 = \frac{1}{8}(-5j + 4j^2 - 2\alpha D + 4j\alpha D + \alpha^2 D^2)b_{1/2}^{(j)}(\alpha), \quad (15)$$

$$f_2 = \frac{1}{8}(2 - 7j + 4j^2 - 2\alpha D + 4j\alpha D + \alpha^2 D^2)b_{1/2}^{(j-2)}(\alpha) - \frac{27}{8}\alpha, \quad (16)$$

where $j = 3$ for the 3:1 resonance, $\alpha = a_1/a_2$ is the ratio of semimajor axes, and $D = d/d\alpha$ is the differential operator. The quantity $-27\alpha/8$ in Equation (16) is the indirect term for the case when $M_2 > M_1$.

Using Equations (13) and (14), we calculate the critical eccentricities to be $e_{1,\text{crit}} = 0.00864$ and $e_{2,\text{crit}} = 0.00410$. Even for initial e_1 values that are low (e.g., osculating value of 0.001), $e_1 < e_{1,\text{crit}}$ will not always be satisfied because short-term eccentricity fluctuations due to primary J_2 will inflate e_1 excursions up to ~ 0.014 (assuming $a_1 = 654 \text{ km}$ in Equation (3) of Section 5). For Romulus, marooned farther from the primary such that J_2 effects are lessened, if the pre-encounter eccentricity is low enough then it is possible that the eccentricity will always remain less than the critical eccentricity. These analytical

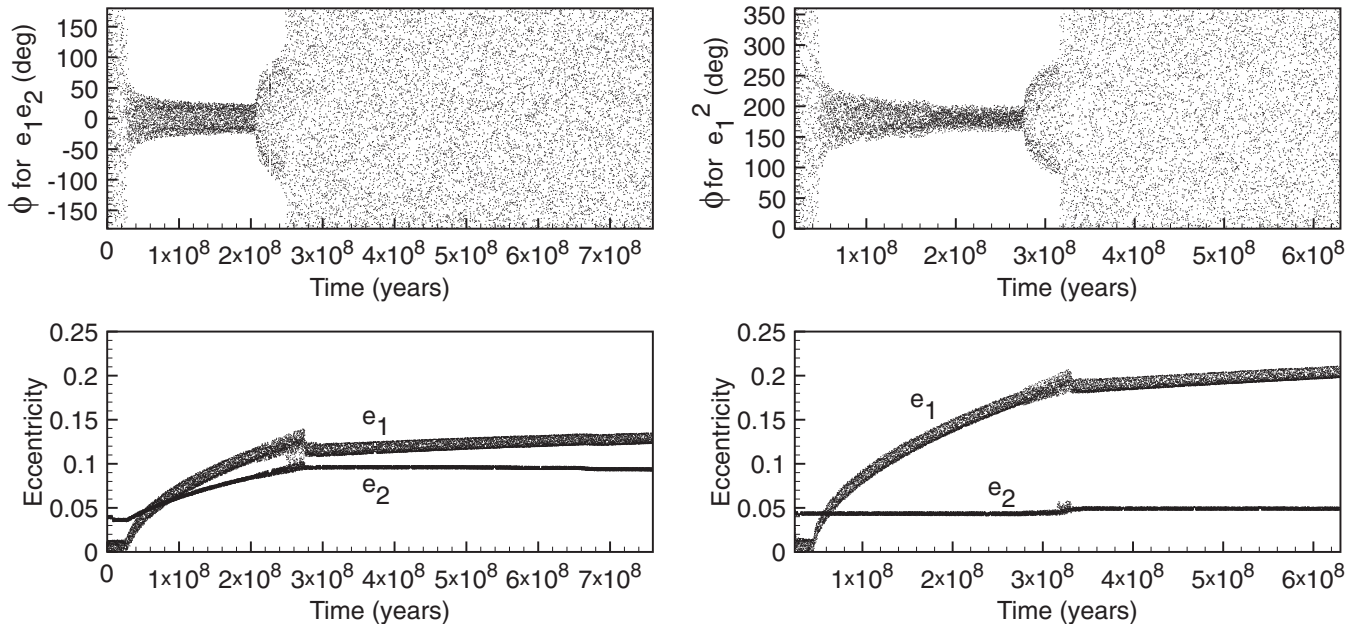


Figure 8. Examples of simulations with temporary resonant capture followed by escape. Dots show results from numerical simulations for the libration angle ϕ and eccentricity e as a function of time. Subscripts 1 and 2 represent the inner and outer satellites, respectively. Left-side plots: results of a simulation with temporary capture into $e_1 e_2$ resonance, where both e_1 and e_2 increase. Initial conditions for eccentricity are $e_1 = 0.001$ and $e_2 = 0.04$. Right-side plots: results of a simulation with temporary capture into e_1^2 resonance, where only e_1 increases. Initial conditions for eccentricity are $e_1 = 0.007$ and $e_2 = 0.04$.

arguments are in agreement with the results from our numerical experiments.

If we contemplate scenarios in which resonant capture never occurred in Sylvia’s past, then we must adopt the critical eccentricities as lower limits on the past eccentricities of Remus and Romulus. Their past eccentricities cannot be lower than these limits because otherwise capture would have been guaranteed. We note that these lower limit eccentricities are lower than the nominal observed eccentricities (Table 4), and hence this evolutionary pathway is a plausible scenario without requiring any significant modifications in eccentricity over time.

To summarize these results, from these three pathways we find that both (1) temporary capture followed by escape and (2) no capture are plausible scenarios that occurred when Remus and Romulus encountered 3:1 resonance. If pathway (1) occurred, our calculations of the necessary damping required to bring post-resonance eccentricities to observed values show this is possible for Remus but may be prohibitively long for Romulus, depending on its post-resonance eccentricity. Therefore, it is unlikely that a substantial increase in the eccentricity of Romulus occurred, even if the system was temporarily captured in the e_2^2 or $e_1 e_2$ resonances. If pathway (2) occurred, we can set lower limits on past eccentricities of both satellites to be equal to their critical eccentricities.

7. CONCLUSIONS

The goals of this study were to characterize Sylvia’s current orbital configuration and masses as well as to illuminate the past orbital evolution of this system. Our work can be summarized as follows.

1. We reported new astrometric observations of Sylvia in 2011 that increased the number of existing epochs of astrometry by over 50%. These new observations extended the existing baseline of observations to 7 years for Remus and to 10 years for Romulus.

2. We fit a fully dynamical three-body model to the available astrometric data. This model simultaneously solved for orbits of both satellites, individual masses, and the primary’s oblateness (Table 4). We found that the primary has a density of $1.29 \pm 0.39 \text{ g cm}^{-3}$ and is oblate with a J_2 value in the range of 0.0985–0.1. Constraints on satellite radii can be obtained from the mass determinations by assuming that the satellites have a bulk density equal to that of the primary; we find ~ 4.5 – 6.1 km for Remus and ~ 2.6 – 8.2 km for Romulus. These ranges would have to be modified if the actual density of the primary or of the satellites was different from the nominal value assumed here. The orbits of the satellites are relatively circular. We find that the primary’s spin pole is best fit when aligned to Romulus’ orbital pole, and that the satellites’ orbit poles are coplanar to within 1 deg.
3. We numerically investigated the short-term and long-term stability of the orbits of Sylvia’s satellites. There are periodic fluctuations in eccentricity for both satellites, most notably for the inner satellite Remus. We verified that these eccentricity excursions are due to the effects of primary oblateness. From long-term integrations we found that the system is in a very stable configuration, in agreement with previous investigations.
4. We studied the past orbital evolution of Sylvia’s satellites, including the most recent low-order mean-motion resonance crossing, which is 3:1. We used direct N -body integrations with forced tidal migration to model such an encounter. To examine the case of resonant capture followed by escape, we calculate the tidal damping timescale to go from the post-encounter eccentricity to the observed value. Using available tidal models, we find that the damping timescale for Romulus can be prohibitively large if its post-resonance eccentricity exceeded ~ 0.023 . This suggests that the system crossed the e_2^2 and $e_1 e_2$ resonances without capture, or that it was not captured in these

resonances for a sufficient duration to substantially increase the eccentricity of Romulus. Similar timescale constraints from tidal damping also imply that Remus may have a rubble pile structure if its post-resonance eccentricity exceeded ~ 0.032 . Alternatively, if no capture in any resonance occurred then we are able to set lower limits on their past eccentricities ($e_1 = 0.00864$ and $e_2 = 0.00410$).

The detailed characterization of Sylvia presented in this paper has allowed for analyses of its orbital evolution. Such studies of triple systems are important in order to understand their key physical properties, orbital architectures, and intriguing evolutionary histories.

We thank Stan Peale, Man Hoi Lee, and Fred Davies for useful discussions. We are grateful to the reviewer for helpful comments.

Some of the data presented herein were obtained at the W. M. Keck Observatory, which is operated as a scientific partnership among the California Institute of Technology, the University of California, and the National Aeronautics and Space Administration. The Observatory was made possible by the generous financial support of the W. M. Keck Foundation. The authors wish to recognize and acknowledge the very significant cultural role and reverence that the summit of Mauna Kea has always had within the indigenous Hawaiian community. We are most fortunate to have the opportunity to conduct observations from this mountain. This work was based in part on observations made with ESO telescopes at the La Silla Paranal Observatory under program ID 088.C-0528. This research was done using resources provided by the Open Science Grid (OSG), which is supported by the National Science Foundation and the U.S. Department of Energy's Office of Science. We thank Mats Rynga for his assistance with the OSG.

This work was partially supported by NASA Planetary Astronomy Grant NNX09AQ68G.

REFERENCES

- Benecchi, S., Noll, K., Grundy, W., & Levison, H. 2010, *Icarus*, **207**, 978
- Bottke, W. F., Durda, D. D., Nesvorný, D., et al. 2005, *Icarus*, **179**, 63
- Brouwer, D. 1959, *AJ*, **64**, 378
- Brown, M. E., Bouchez, A. H., Rabinowitz, D., et al. 2005, *ApJ*, **632**, L45
- Brown, M. E., & Margot, J. L. 2001, *IAU Circ.*, **7588**, 1
- Brown, M. E., van Dam, M. A., Bouchez, A. H., et al. 2006, *ApJ*, **639**, L43
- Brozovic, M., Benner, L. A. M., Nolan, M. C., et al. 2009, *IAU Circ.*, **9053**, 2
- Cash, W. 1976, *A&A*, **52**, 307
- Chambers, J. E. 1999, *MNRAS*, **304**, 793
- Čuk, M. 2007, *ApJ*, **659**, L57
- Čuk, M., & Burns, J. A. 2005, *Icarus*, **176**, 418
- Descamps, P., Marchis, F., Berthier, J., et al. 2011, *Icarus*, **211**, 1022
- Drummond, J., & Christou, J. 2008, *Icarus*, **197**, 480
- Fang, J., Margot, J.-L., Brozovic, M., et al. 2011, *AJ*, **141**, 154
- Farinella, P., Vokrouhlický, D., & Hartmann, W. K. 1998, *Icarus*, **132**, 378
- Ferraz-Mello, S., Beaugé, C., & Michtchenko, T. A. 2003, *Celest. Mech. Dyn. Astron.*, **87**, 99
- Frouard, J., & Compere, A. 2012, *Icarus*, **220**, 149
- Goldreich, P. 1963, *MNRAS*, **126**, 257
- Goldreich, P., & Sari, R. 2009, *ApJ*, **691**, 54
- Goldreich, P., & Soter, S. 1966, *Icarus*, **5**, 375
- Greenberg, R. 1981, *AJ*, **86**, 912
- Jacobson, S. A., & Scheeres, D. J. 2011, *ApJ*, **736**, L19
- Kaasalainen, M., Torppa, J., & Piironen, J. 2002, *Icarus*, **159**, 369
- Kryszczyńska, A., La Spina, A., Paolicchi, P., et al. 2007, *Icarus*, **192**, 223
- Lee, M. H., & Peale, S. J. 2002, *ApJ*, **567**, 596
- Lee, M. H., & Peale, S. J. 2006, *Icarus*, **184**, 573
- Lenzen, R., Hartung, M., Brandner, W., et al. 2003, *Proc. SPIE*, **4841**, 944
- Lin, C.-L., Zhang, Z.-W., Chen, W. P., et al. 2009, *PASP*, **121**, 359
- Marchis, F., Baek, M., Descamps, P., et al. 2007, *IAU Circ.*, **8817**, 1
- Marchis, F., Descamps, P., Dalba, P., et al. 2011, in EPSC-DPS Joint Meeting 2011, 2011 October 2–7, Nantes, France, 653 (<http://meetings.copernicus.org/epsc-dps2011>)
- Marchis, F., Descamps, P., Hestroffer, D., et al. 2005, *IAU Circ.*, **8582**, 1
- Marchis, F., Pollock, J., Pravec, P., et al. 2008, *IAU Circ.*, **8928**, 4
- Margot, J. L., & Brown, M. E. 2001, *BAAS*, **33**, 1133
- Margot, J. L., Brown, M. E., Trujillo, C. A., Sari, R., & Stansberry, J. A. 2005, *BAAS*, **37**, 737
- Margot, J. L., Nolan, M. C., Benner, L. A. M., et al. 2002, *Science*, **296**, 1445
- Markwardt, C. B. 2009, in ASP Conf. Ser. 411, *Astronomical Data Analysis Software and Systems XVIII*, ed. D. A. Bohlender, D. Durand, & P. Dowler (San Francisco, CA: ASP), 251
- Merline, W. J., Close, L. M., Dumas, C., et al. 1999, *Nature*, **401**, 565
- Merline, W. J., Close, L. M., Siegler, N., et al. 2002, *IAU Circ.*, **7827**, 2
- Meyer, J., & Wisdom, J. 2008, *Icarus*, **193**, 213
- Murray, C. D., & Dermott, S. F. 1999, *Solar System Dynamics* (Cambridge: Cambridge Univ. Press)
- Naidu, S. P., Margot, J. L., Busch, M. W., et al. 2011, in EPSC-DPS Joint Meeting, Vol. 6
- Nolan, M. C., Howell, E. S., Becker, T. M., et al. 2008, *BAAS*, **40**, 432
- Noll, K. S., Grundy, W. M., Chiang, E. I., Margot, J.-L., & Kern, S. D. 2008, in *Binaries in the Kuiper Belt*, ed. M. A. Barucci, H. Boehnhardt, D. P. Cruikshank, A. Morbidelli, & R. Dotson (Tucson, AZ: Univ. Arizona Press), 345
- Ostro, S. J., Margot, J. L., Benner, L. A. M., et al. 2006, *Science*, **314**, 1276
- Press, W. H., Flannery, B. P., Teukolsky, S. A., & Vetterling, W. T. 1992, *Numerical Recipes in C: The Art of Scientific Computing* (New York: Cambridge Univ. Press)
- Ragozzine, D., & Brown, M. E. 2009, *AJ*, **137**, 4766
- Rousset, G., Lacombe, F., Puget, P., et al. 2003, *Proc. SPIE*, **4839**, 140
- Shepard, M. K., Margot, J. L., Magri, C., et al. 2006, *Icarus*, **184**, 198
- Storrs, A., Vilas, F., Landis, R., et al. 2001, *IAU Circ.*, **7590**, 3
- Tholen, D. J., Buie, M. W., Grundy, W. M., & Elliott, G. T. 2008, *AJ*, **135**, 777
- Vokrouhlický, D., Nesvorný, D., Bottke, W. F., & Morbidelli, A. 2010, *AJ*, **139**, 2148
- Weaver, H. A., Stern, S. A., Mutchler, M. J., et al. 2006, *Nature*, **439**, 943
- Winter, O. C., Boldrin, L. A. G., Vieira Neto, E., et al. 2009, *MNRAS*, **395**, 218
- Zhang, K., & Nimmo, F. 2009, *Icarus*, **204**, 597